Imaging in turbid media using quasi-ballistic photons

Venkatesh Gopal[1], Sushil Mujumdar[2], Hema Ramachandran[2] and A.K.Sood.[1,3]

[1]Department of Physics, Indian Institute of Science, Bangalore 560 012, INDIA
[2]Raman Research Institute, Sadashivanagar, Bangalore 560 080, INDIA
[3]Jawaharlal Nehru Centre for Advanced Scientific Research,
Jakkur Campus, Bangalore 560 066, INDIA

Abstract

We study by means of experiments and Monte Carlo simulations, the scattering of light in random media, to determine the distance upto which photons travel along almost undeviated paths within a scattering medium, and are therefore capable of casting a shadow of an opaque inclusion embedded within the medium. Such photons are isolated by polarisation discrimination wherein the plane of linear polarisation of the input light is continuously rotated and the polarisation preserving component of the emerging light is extracted by means of a Fourier transform. This technique is a software implementation of lock-in detection. We find that images may be recovered to a depth far in excess of what is predicted by the diffusion theory of photon propagation. To understand our experimental results, we perform Monte Carlo simulations to model the random walk behaviour of the multiply scattered photons. We present a new definition of a diffusing photon in terms of the memory of its initial direction of propagation, which we then quantify in terms of an angular correlation function. This redefinition yields the penetration depth of the polarisation preserving photons. Based on these results, we have formulated a model to understand shadow formation in a turbid medium, the predictions of which are in good agreement with our experimental results.

1 Introduction

Photons travelling through turbid media such as milk or clouds are multiply scattered. The turbidity of such media increases with either a high refractive index contrast between the scatterers and the medium, or a large number density of scatterers, or both. What does it mean to be able to 'see' through such a medium?. By the process of 'seeing', one refers to the collection of 'image bearing' photons by the eye, photons that have emerged, despite being scattered, after travelling nearly undeviated from the direction in which they entered the medium. The number of such photons depends on the number density and scattering anisotropy of the scatterers. With very high scatterer concentrations, one has a situation where the number of image bearing photons is nearly negligible and most of the photons have little or no memory of their initial direction of propagation. The transport of the photon density in such a highly multiply scattering regime, can be accurately modelled by a diffusion equation. Measurements of this diffuse intensity can be used to extract useful dynamical information about the medium as in diffusing wave spectroscopy (DWS) [1], or to detect static and dynamic inclusions within the medium [2, 3, 4].

Most methods of selecting such image bearing photons rely on time-gated detection, which utilises the fact that image bearing photons are the first to emerge from the medium while diffusing photons travel much longer paths and emerge later [5]. However, photons also carry information in the form of their state of polarisation and the image bearing photons may be discriminated from those that have travelled longer paths by detecting their polarisation. The initial state of polarisation is preserved for photons travelling nearly straight line trajectories while it is randomised for diffusing photons that have traversed the medium by a random walk. This fact has been recognised and experiments using a

variety of methods to tag these photons [6, 7, 8, 9] have been performed. In a recent experiment [10], light passing through a rotating linear polariser was made incident on a turbid medium. The emerging scattered light, after passing through a fixed analyser, was collected by a detector by scanning across the exit face of the sample. Two pinholes, one before and another after the sample, permitted predominantly the image bearing photons to be detected. The resultant signal consisted of an oscillatory component due to the photons that still retained a significant amount of their original state of polarisation, riding on a constant background arising from the multiply scattered and completely depolarised light. Using lock-in detection to collect only the oscillatory component, it was possible to image millimeter sized objects immersed in milk. In a subsequent experiment [11], the input and exit pinholes were replaced by a lens-aperture system, and the point detector by a CCD camera. The lens aperture system rejects much of the diffuse light while the CCD array permits simultaneous two-dimensional data collection. The frequency lock-in was achieved by means of software and images of objects hidden in turbid media were obtained with high resolution without having to perform multiple scans across the object as in [10].

Before we proceed further, we provide a brief introduction to multiple scattering theory to describe the relevant quantities and notation. Photons entering a scattering medium travel exponentially distributed ballistic pathlengths between scattering events. The scattering mean free path l_s is the mean distance between scattering events and is determined by the scattering cross section σ and the number density ϕ of the scatterers as $l_s = 1/\sigma\phi$. The scattering cross sections and the probability to scatter at a given angle are calculated by the well known Mie theory [12]. However, scattering does not always randomise the direction of the photon. Typically, particles whose sizes are large or comparable to the wavelength of the incident light cannot be thought of as simple dipole scatterers and Mie theory shows that the scattering is strongly peaked in the forward direction (See [13] for a simple description of why this must be so). The result of this anisotropy in scattering is that the photon is often not randomised after a single scattering event and there is a 'persistence length' over which the photon travels, on average, in approximately the same direction before being randomised. If the photon undergoes a very large number of scattering events, then one may assume that the photon performs a random walk and that the photon flux is transported diffusively within the medium. The persistence length or the length scale over which the photon is randomised is called the transport mean free path l^* [14]. The 'optical thickness' or optical density τ of a slab of thickness L is defined as $\tau = L/l^*$. When $L \sim l^*$ the scattering is largely ballistic, and, when $L \gg l^*$, the diffusion approximation is valid [1, 14]. The scattering anisotropy g, a measure of the persistence length, is defined in terms of the mean free paths l^* and l_s as $g = 1 - (l_s/l^*)$.

Photons travelling through a random medium may be classified into three types: a ballistic component that has not undergone any scattering, a diffuse component that is completely randomised directionally and may be modelled by a diffusion equation, and a quasi-ballistic or 'snake' component, that has undergone more than one scattering event but is still travelling in approximately the same direction as it did when it entered the medium. The ballistic and snake photons together form the image bearing component of the transmitted intensity. The ballistic transmitted intensity falls off exponentially with the thickness L of the scattering medium as $I_{ballistic} = \exp(-L/l_s)$ and is usually too small to detect at large optical densities. However images with high resolution may still be acquired using the snake photons. The snake component is intermediate between the ballistic and diffuse regimes and is currently poorly understood. This crossover from one regime to another has often been modelled in an approximate manner by assuming that a delta function source of diffusing photons lies at a fixed depth within the medium. This approximation yields excellent results when the detector collects only diffuse light but fails rather significantly otherwise [15, 16]. Our motivation in the present work is twofold. First, we seek to understand how far one can 'see' into a random medium using snake photons, and to place limits on the depth to which such snake photon imaging can be

performed. The second is to investigate the crossover from the ballistic to the diffusive regime, and thus to understand the characteristics of the quasi-ballistic photons.

2 Experimental details

2.1 Apparatus

A schematic diagram of the experimental apparatus is shown in Fig.1. Light from a 2.5 mW, randomly polarised Helium-Neon laser (Melles-Griot, λ=612 nm) is expanded and collimated. The laser beam passes through a polariser **RP** that is coupled to a stepper motor driver which rotates the polaroid through 360^o in a variable number of steps. The central part of the expanded and collimated beam is selected by an iris diaphragm and made incident on a metal mask **MM** with a 3 mm diameter hole cut into it. Thus, a circular spot of light of nearly uniform intensity is incident on the cuvette **S** containing a colloidal suspension. The cuvette has an internal thickness of 10mm. After passing through the scattering medium, the transmitted light is collected by the lens **L1**. The light passing through the lens is apertured by another iris diaphragm **PH**, which rejects a large fraction of the diffuse flux that would otherwise be incident on the CCD camera. The light transmitted through this aperture then passes through a fixed analysing polaroid **FA** and is incident on an intensified, variable gain CCD camera. The camera has an 8 bit (256 grayscale values) intensity resolution with a 512 $\times$ 512 pixel array.

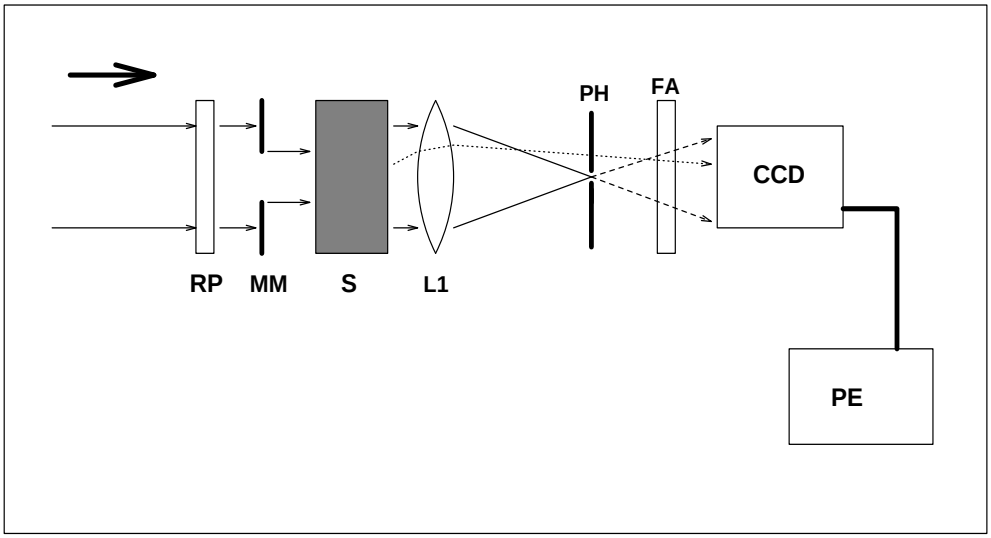

Figure 1: Schematic diagram of the experimental apparatus. **RP** : Rotating polaroid, **MM** : Metal mask with 3 mm diameter hole, **S** : Cuvette containg scattering medium, **L1** : Lens (f = 90 mm), **PH** : Aperture , **FA** : Fixed analyser, **CCD** : Intensified CCD camera with variable gain, **PE** : Processing electronics.

It can be seen from Fig. 1 that in the absence of the colloidal suspension, parallel rays of the incoming beam, on passing through the lens **L1**, converge to a focus at the aperture **PH** and then diverge to form a spot on the CCD. The size of the spot is determined by the focal length of **L1** and the distance of the CCD from **PH**. On interposing the colloidal suspension, lens **L1** then images not only the snake photons that emerge normal to the face of the cuvette, but also some fraction of the diffusively scattered light that emerges along paths parallel to the snake photons. Since, in the

absence of the pinhole diffuse photons that emerge at angles not normal to the cuvette would also be imaged onto the CCD array, it was necessary to limit the acceptance angle of the detector with an aperture. The dotted line in Fig. 1 shows one such a photon trajectory which would be incident on the detector if it were not rejected by the aperture **PH**.

The experiment is performed as follows. First, a direct image without the sample is recorded to serve as a reference. A sample image obtained is shown in Fig.2. The concentric diffraction rings seen in the image are due to diffraction from the edges of the mask **MM**. The dark region at the top right of the bright spot of light, is due to a defect on one of the optical components. The cuvette with the colloidal suspension is now introduced into the beam. To ensure that the maximum dynamic range of the detector is used, the polarisers are crossed and the gain is increased such that, on making the two polaroids parallel, the pixels in the brightest region of the image are almost saturated. However, as the diffuse flux begins to increase at high optical densities, the baseline intensity, the intensity when the polarisers are crossed, is not zero any longer. The amplitude of the intensity oscillations rapidly decreases beyond this point as the snake photon population is sharply reduced and the diffuse flux begins to dominate the scattered intensity. The polariser RP is rotated in steps of 15^o and at each step an image is recorded and saved. The process is continued until 512 frames are recorded. Experiments were performed for each of the colloidal suspensions of the following optical densities : $\tau = 0.5$, 1.1, 2.5, 3.0, 3.6, 5.2, 5.9, 6.7, 8.8, 9.5, 10.5, 11.6 , and 12.6, which were prepared using $0.23\mu m$ diameter polystyrene particles (Bangs Laboratories, U.S.A.) suspended in water. At $612nm$, these particles were calculated to have a scattering anisotropy, $g = 0.45$.

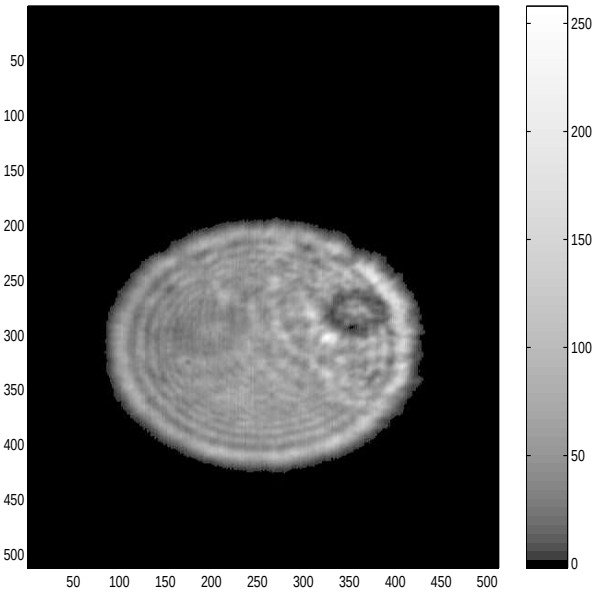

Figure 2: Direct image of the laser beam recorded without the scattering medium.

2.2 Data Processing

Figure 3 shows in schematic form, the procedure for processing the images. At the end of each run, we obtain a deck of 512 frames ordered in time. Consider any pixel from an image of this deck, say the pixel $P_k(i, j)$. The indices i and j refer to the location of the pixel within the kth image of the deck. A time series is formed for the (i, j)th pixel by storing all the time ordered values that this

pixel takes as the polaroid **RP** is rotated. This time series is then Fourier transformed using a Fast Fourier Transform (FFT) routine which yields two peaks, one at zero frequency, and another at the rotational frequency of the polaroid, $\omega = \pi/N_s$ ($N_s = 12$, the number of images in one half rotation of the polaroid, after which the signal repeats itself). The amplitudes of the zero frequency peak and that at the rotational frequency are stored and two separate images are built up. In one image, termed as the 'zero frequency' image, the pixel with coordinates (i, j) is assigned the value of the amplitude of the peak at zero frequency. In the other image, the pixel with coordinates (i, j) is assigned the amplitude of the peak obtained at the rotation frequency. This image is termed the 'polarisation retaining' image.

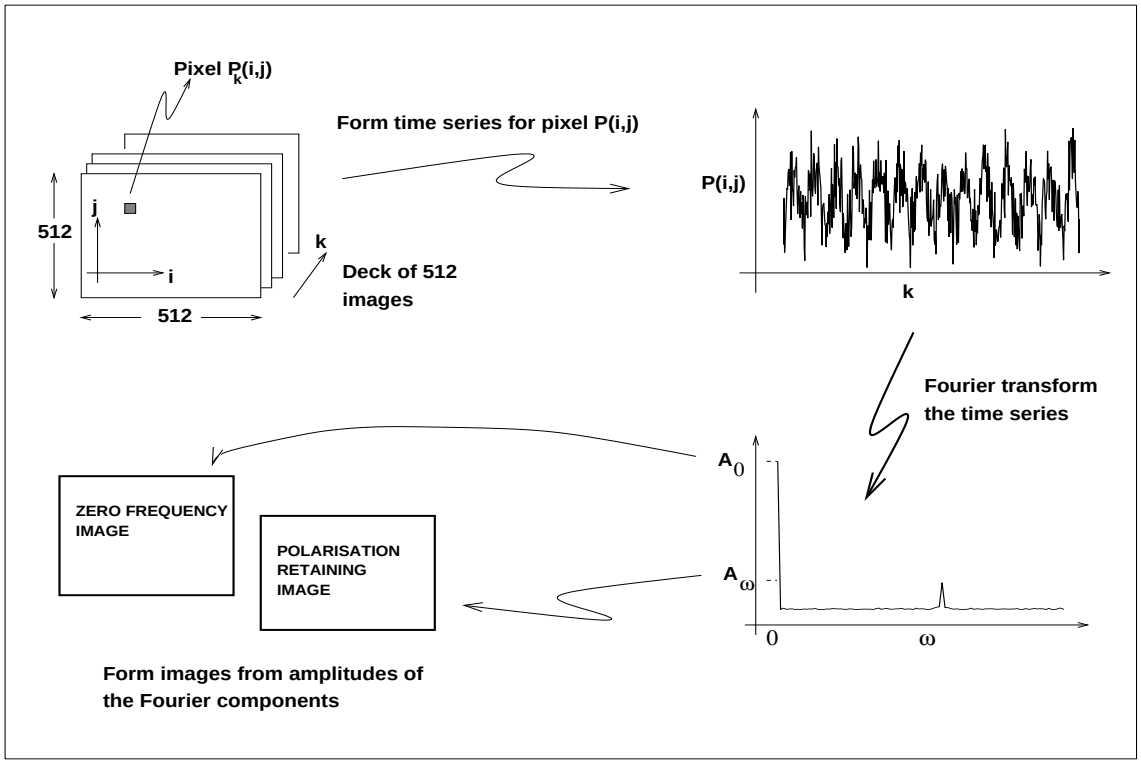

Figure 3: Schematic representation of the data processing procedure. $\mathbf{A_0}$ and $\mathbf{A}_\omega$ are the Fourier amplitudes at the zero and the polaroid rotational frequencies respectively.

3 Experimental results

We have imaged the bright spot of light that is transmitted by the metal mask **MM** through colloidal suspensions of $0.23\mu m$ particles of a wide range of optical densities. While a direct image was seen in the optically thin samples ($\tau <\sim 7$), no image was directly discernible at larger τ. However, on processing the data as described earlier, the circular spot of light was visible in the polarisation retaining image and images could be extracted upto $\tau \sim 10$. Figure 4 shows a series of images obtained at optical densities of 5.94 (figs. a & b), 8.76 (figs. c & d) and 9.54 (figs. e & f). The images on the left are the polarisation retaining images , while those on the right are the zero frequency images. Figures 4(c-f) have been smoothened by applying a 10×10 median filter to improve the contrast and remove some of the noise .In figs. 4(e) and 4(f), the camera has been moved closer to the aperture and so the bright transmitted spot of light is smaller than in the previous images. These images are recorded at high gain levels of the CCD camera and are noisy because the CCD array is extremely

sensitive to stray light at high gain. That we have not been entirely successful in cutting off all stray light is evident from the bright streaks that can be seen at the top and bottom of some of the images .Figures 4(c) and 4(e) clearly bring out the efficacy of the technique .While the zero frequency image 4(d) faintly shows a part of the outline of the bright disc, and 4(f) shows no details at all, a clear image is visible in the corresponding polarsation retaining images 4(c) and 4(e).

We have studied the variation of the quality of the images obtained as a function of the optical density of the scattering medium. A number of parameters could be used to quantify the quality of an image, such as the sharpness of the edges, or the visibility of features within the image. However, we are interested in determining the fraction of the transmitted photons that preserve their polarisation, as a function of the optical density of the medium. Therefore, we measure for each pixel, the ratio of the Fourier amplitudes $\mathbf{R} = A_\omega/A_0$. Here A_0 is the amplitude of the zero frequency component, and A_ω the amplitude of the rotational frequency component obtained on Fourier transforming the time series for a given pixel. The ratio $\mathbf{R}$ is calculated and averaged for each pixel within a region of approximately 200 $\times$ 200 pixels, which is chosen at the centre of the circular transmitted spot of light. The pixels in our camera are rectangular causing the circular spot of light transmitted by the mask to appear oval in the images. Since the shape of the object is not important to our analysis, we do not correct for this distortion of the aspect ratio.

To understand the parameter $\mathbf{R}$ better, consider two limiting cases of imaging, one in which the medium is transparent with no scattering, and at the other extreme, one in which the entire scattered flux is diffuse and the number of quasi-ballistic photons is negligible. The scattered light may be thought of as consisting of a polarised component whose intensity varies as $\cos^2\theta$, where θ is the relative angle between the rotating polaroid and the fixed analyser, and a randomly polarised diffuse component of constant intensity. The signal in the case of a transparent medium consists of only an oscillatory component. The ratio of the Fourier amplitudes in this case would then be given by $\mathbf{R} = 0.5$ as can be seen from our choice of definition of the Fourier coefficients [17]. In other words, for a purely oscillatory signal, the mean is half the peak-to-peak swing of the signal. In the case of a highly turbid medium, we have a constant intensity at any orientation of the rotating polaroid and $\mathbf{R} = 0$.

Figure 5 shows the variation of $\mathbf{R}$ with increasing optical density τ. We observe that upto $\tau \sim 7$ there is almost no variation in $\mathbf{R}$ and it is also very close to the maximum value of 0.5 that can be attained for a signal consisting of *only* the time varying component. For the range $7 < \tau < 10$ we observe an exponential decay in R, while beyond $\tau > 10$ the ratio remains constant and no images could be extracted. These results are rather surprising for two reasons. First, according to the diffusion model commonly employed, it is assumed that photons are randomised on a length scale comparable to l^*. In fact, in deriving an expression for the diffuse flux that crosses a given area element in a random medium, it is assumed [18], that the probability for a photon to travel a path length s without being randomised is given by $P(s) = \exp(-s/l^*)$. Thus diffusion theory would predict that the non-randomised or image bearing flux at a depth of $7l^*$ would be only a fraction $\sim 9 \times 10^{-4}$ of the incident flux. As we show later, this fraction would be comparable to the diffuse background intensity, making R much less than 0.5. Secondly, one would expect a gradual decrease in $\mathbf{R}$ and not the abrupt change that is observed since there is a smooth conversion of photons from quasi-ballistic to diffusive transport.

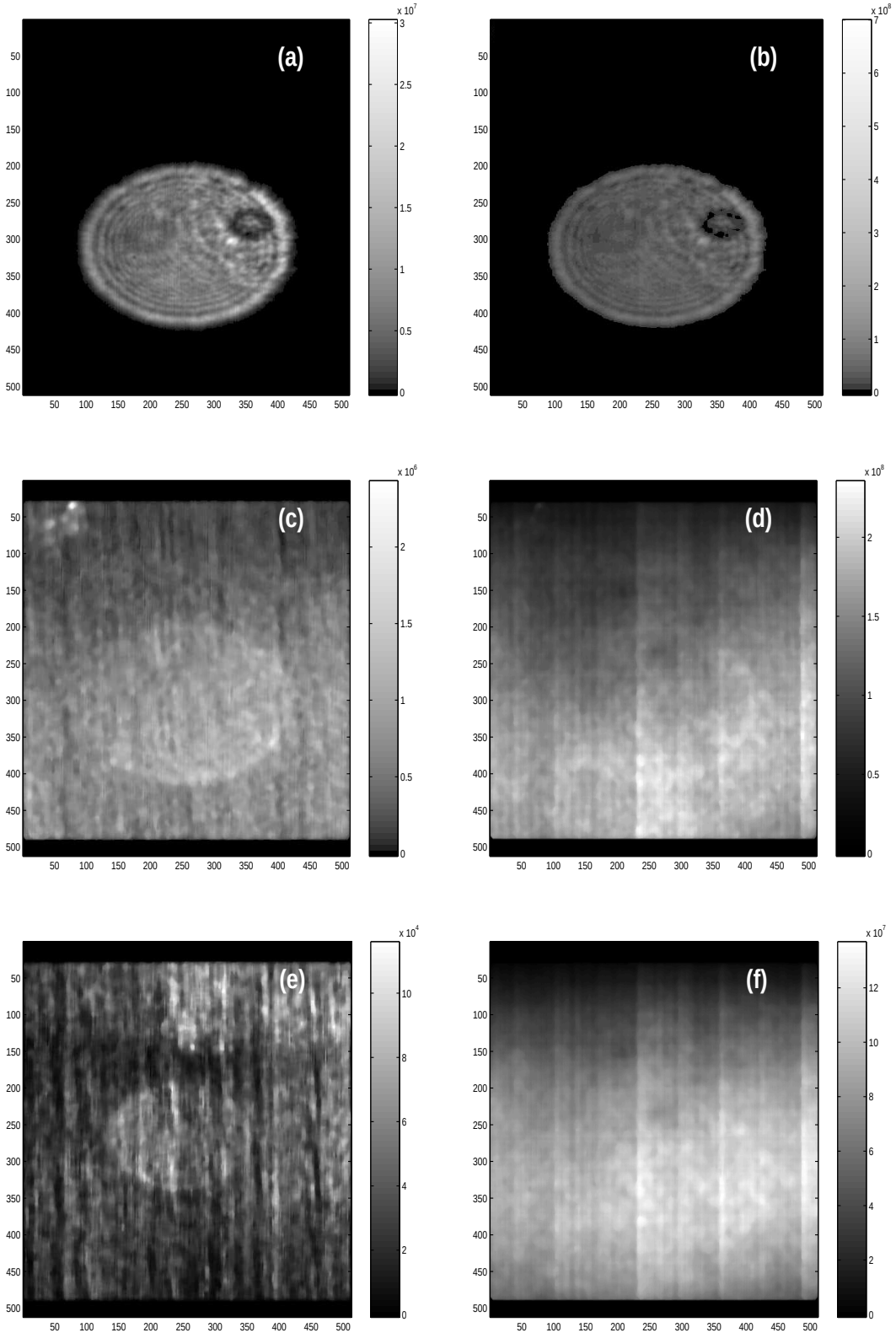

Figure 4: Images recorded at the following optical densities (a,b) $\tau = 5.94$, (c,d) $\tau = 8.76$ and (e,f) $\tau = 9.54$. The polarisation preserving images ((a),(c), and(e)) are in the column on the left while the zero frequency images ((b),(d), and(f)) are in the one on the right.

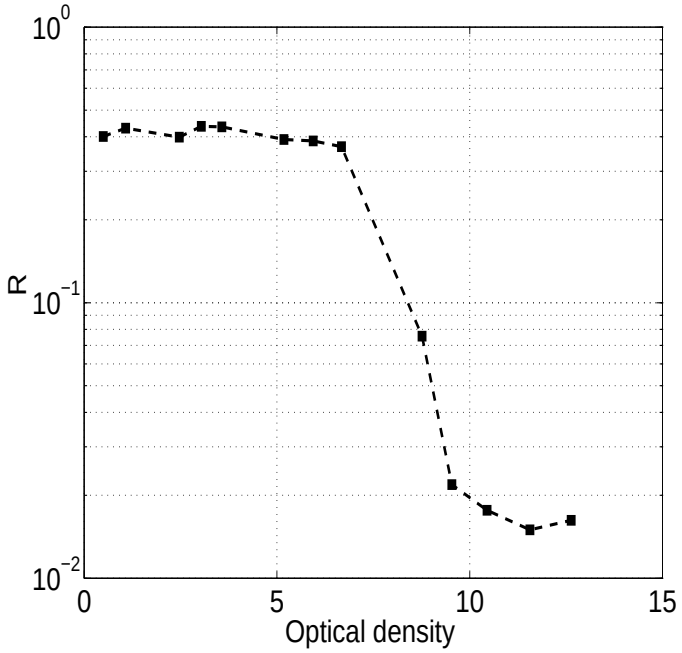

Figure 5: Variation of the image visibility parameter $\mathbf{R} = A_\omega/A_0$, as a function of the optical density $\tau = L/l^*$.

4 Discussion

Our aim now is to explain our results within the framework of a simple model that would provide order-of-magnitude estimates of the visibility of images obtained through random media. On the one hand, when the scattering is minimal ($\tau <\sim 3$), the analysis is simple, and on the other, in the highly multiple scattering limit too, solutions can be found by a suitable application of the diffusion equation. However, the nearly constant value of $\mathbf{R}$ upto $\tau \sim 7$ urges us to reconsider our understanding of what constitutes a 'diffuse' photon. In this section we describe results obtained by Monte Carlo random walk simulations of photon transport in scattering media. These simulations are central to the understanding of our experimental results.

4.1 Monte Carlo simulations

The procedure for our Monte Carlo simulations was as follows. Photons were launched from the centre of an infinite slab. The simulation modelled photon transport assuming that the photons travel exponentially distributed lengths s between scattering events. The probability $P(s)$ of travelling a ballistic path length s is given by the familiar Lambert-Beer law, $P(s) = exp(-s/l_s)$, where l_s is the scattering mean free path of the photons in the medium. The random paths between scattering events were generated taking $s = -l_s \cdot \ln(RAN)$, where RAN is a random number uniformly distributed between 0 and 1 [19]. The scattering angles were chosen such that they had a distribution of directions given by the Henyey-Greenstein phase function [15], where the probability of scattering at an angle θ relative to the incident direction of the photon is given by

$$P(\cos\theta) = \frac{1-g^2}{(1+g^2-2g\cos\theta)^{3/2}} \tag{1}$$

4.2 Defining a diffusing photon

In the spirit of diffusion theory, we assume that a diffuse photon is one which has lost all memory of its initial direction of propagation. The scattering anisotropy is a measure of the ability of a photon to 'remember' its initial direction after a single scattering event. For a scattering anisotropy $g = 1$, the photon always travels along its initial direction of propagation, while for $g = 0$, it is randomised at each scattering event. We have used random walk simulations to investigate the variation of the number of scattering events that it takes for the direction of the incident photon to be completely randomised, as a function of the scattering anisotropy. Photon trajectories were generated, as described previously, in an infinite medium. The directional correlation function $C(j) = \langle \hat{\mathbf{n}}(0) \cdot \hat{\mathbf{n}}(j) \rangle$, where $\hat{\mathbf{n}}(j)$ represents the unit vector along the photon trajectory after the jth scattering event, was calculated for eight different values of g, averaging over 10^4 trajectories in each case. A plot of $C(j)$ is shown in Fig. 6 for three values of g. At long times, $C(j)$ fluctuates about zero. We calculate the standard deviation in the fluctuations of $C(j)$ at long times and then find the point where $C(j)$ drops below this value for the first time. This value of j is taken as the number of scattering events N_d required for a complete loss of angular correlation. It can be seen from Fig. 6, that for isotropic scatterers it takes only a few (~ 3 for $g = 0.06$) events for angular memory to be lost, while on the other hand, the anisotropic scatterers require many more scattering events (~ 9 for g $= 0.42$ and ~ 17 for $g = 0.72$). This however, yields no information about the length scale over which the photons undergo N_d scattering events, and naturally, begs the question, how far away from the point at which it is launched, is a photon, when it loses angular memory? We answer this question in the next section.

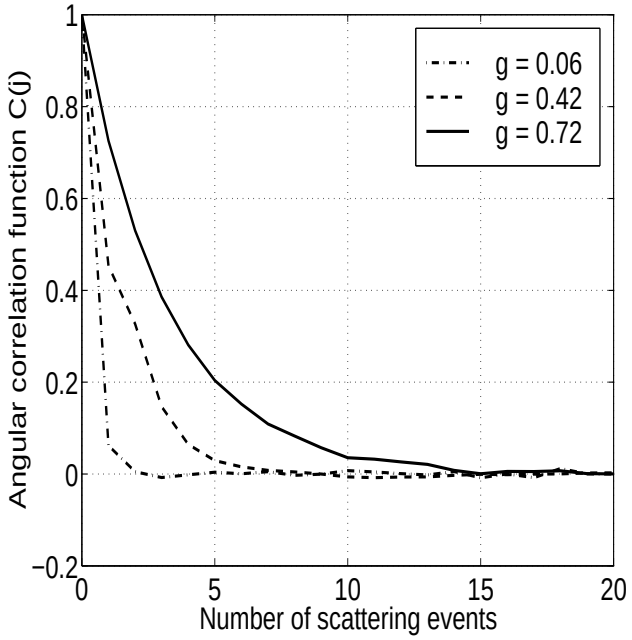

Figure 6: The angular correlation function $C(j) = \langle \hat{\mathbf{n}}(0) \cdot \hat{\mathbf{n}}(j) \rangle$ is shown as a function of the number of scattering events j, for three different values of the scattering anisotropy g.

4.3 Where is a diffusing photon?

According to diffusion theory, the randomisation of a photon takes place typically after travelling a distance l^*, and usually the source of diffusing photons is modelled by placing a delta function source at a depth of l^* within the medium. However, it is also well known that this assumption, especially when considering photon transmission, is inaccurate when the thickness of the scattering medium is less than about $8l^*$ [20]. Clearly, photons are not randomised at any one single depth inside the medium and obviously there exists a smooth distribution of lengths over which the initially quasi-ballistic flux is converted to a diffusive one.

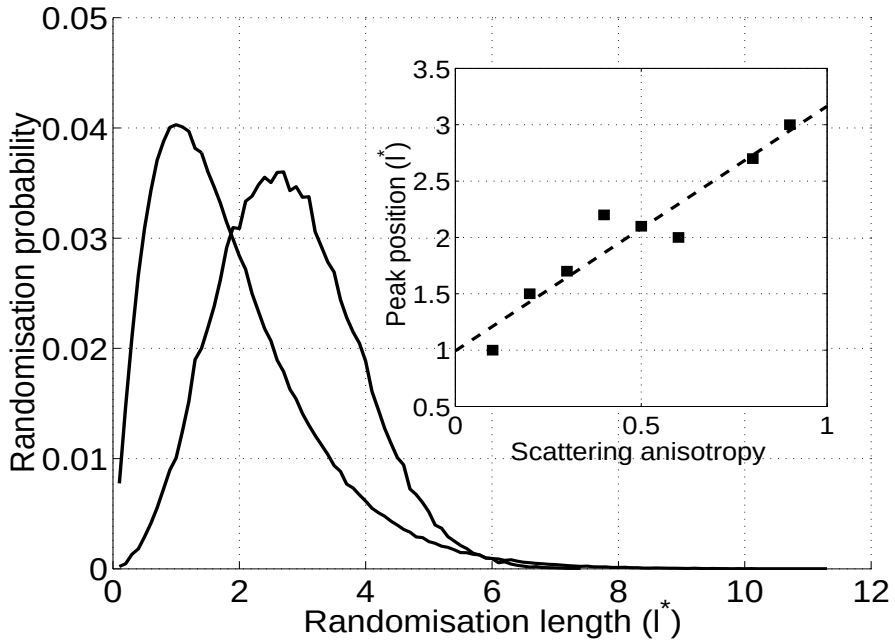

Figure 7: Normalised histograms obtained for the randomisation probability that a snake photon will undergo N_d scattering events, are shown as a function of the distance travelled from the source. This distance is termed the 'randomisation length'. Curves 'a' and 'b' are obtained for scattering anisotropies of 0.1 and 0.8 respectively. The inset shows the variation of the position of the peak of these histograms as a function of the scattering anisotropy.

Random walk simulations for the following anisotropy values : $g = 0.1$, 0.2, 0.3, 0.4, 0.5, 0.6, 0.8 and 0.9, were used to obtain this distribution of lengths. Once again photons were launched from the origin, but in a semi-infinite half-space instead. For a given scattering anisotropy though, we know from the previous simulation, the number of scattering events N_d required for the photon to lose directional memory. The simulation propagated photons as before but terminated the trajectory either when the photon had scattered N_d times, or when the photon had been backscattered out of the half space. Boundary reflections were neglected and absorbing boundary conditions were applied at the back face of the semi-infinite medium. The radial distance travelled from the origin after N_d scattering events was stored and a histogram of the distribution of these radial distances was constructed. The histogram bins had a width of $l^*/10$ and were normalised by the total number of photons that underwent N_d scattering events. In the subsequent discussion, after this normalisation, we treat the number stored in each bin as the randomisation probability for the snake photons. This however is strictly not true and we comment on errors introduced by our choice of normalisation in a later section. It must also be noted here, that by counting only those photons that undergo N_d

scattering events within the medium, we have implicitly 'defined' a snake photon as one that has *not* left the medium before it has scattered N_d times. Once again, the ambiguity inherent in such a definition is overlooked in view of the close agreement obtained with experimental results. Figure 7 shows the distribution of 'randomisation lengths' for scattering anisotropies of 0.1 (curve a) and 0.8 (curve b) The inset shows the peak position of these distributions as a function of g.

In Fig. 7, two features are to be noted. The distribution is sharper for the nearly isotropic scatterers, and, becomes more symmetric as the scattering anisotropy is increased. From the results of the previous section, we know that for $g = 0.1$, only about three scattering events are required for a loss of directional memory, whereas for $g = 0.8$, about 25 scattering events are required. The symmetry and shape of the peaks may now be understood as a consequence of the central limit theorem. To do this, reconsider the simulation as follows. The simulation may be thought of as taking N_d vectors from a set of vectors whose lengths are exponentially distributed as $P(s) = exp(-s/l_s)$, where $P(s)$ is the probability of drawing a vector of magnitude s. The vectors are then placed head to tail at angles that are drawn from a set of angles distributed according to the Henyey-Greenstein function. The histogram is the distribution of lengths of the resultant displacement vectors. For nearly isotropic scatterers, $l^* \sim l_s$, and therefore, for lengths less than a transport mean free path there is a very small probability that a photon will be randomised since it is most likely to be at least one mean free path away from the source after even a single scattering event. Therefore, when N_d is small, the distribution will be peaked approximately at $s \sim l^*$, will exhibit a sharp fall-off for $s < l^*$ and decay more gradually for $s > l^*$. On the other hand, with increasing anisotropy, N_d is much larger. As can be seen from Fig. 6, for $g = 0.8$, only the first 10 or so scattering events are strongly correlated. After that, only a weak directional correlation persists. Thus, when $N_d \sim 10$ or more, the central limit theorem is approximately valid since the correlations are weak and the resultant distribution tends towards a Gaussian and a smoother, broader peak is obtained.

The inset in Fig. 7 shows the positions of the peaks of the randomisation length histograms as a function of the scattering anisotropy. We see that for nearly isotropic scatterers, the peak lies near l^* and moves out to a maximum of about $3l^*$ for a scattering anisotropy of 0.9. Thus, we see that the length scale l^* arises *naturally* when the scattering is almost isotropic and corresponds to the position of the peak of the distribution of randomisation lengths. With increasing anisotropy, the scattering is peaked in the forward direction and the peak of the distribution lies further into the medium.

There is no single randomisation length as supposed by diffusion theory but instead a distribution of lengths over which the conversion to diffusive transport takes place. According to diffusion theory, the average number of scattering events that the photon needs to experience to be randomised is $n = l^*/l_s$. We compare this in Table 1, with the number N_d obtained from our model and find that $N_d \gg n$. Figure 8 shows the data in Table 1 as a graph.

Scattering anisotropy ($g = 1 - l_s/l^*$)	0.1	0.2	0.3	0.4	0.5	0.6	0.8	0.9
$n = l^*/l_s$	1.1	1.25	1.43	1.67	2.0	2.5	5	10
N_d	3	5	6	8	12	14	25	53

Table 1 Comparison of the number of scattering events required to randomise the photon. N_d is calculated from a Monte Carlo simulation while n is the value predicted by diffusion theory.

By integrating the area under the curve for the randomisation probability shown in Fig. 7, we

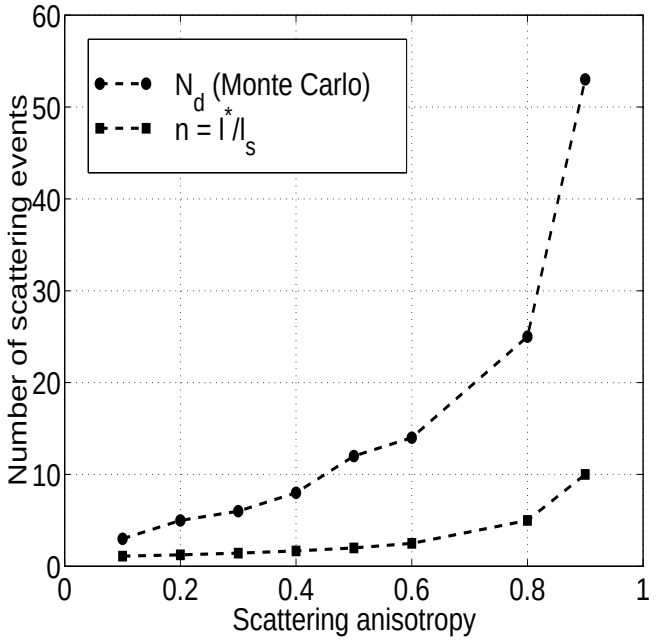

Figure 8: Comparison between $n = l^*/l_s$ and N_d, the average number of scattering events required to randomise the direction of a photon as predicted by diffusion theory and as obtained by Monte Carlo simulations respectively.

obtain the fraction of the snake photon flux that is randomised as a function of the distance travelled from the source. This fraction is denoted by $\mathbf{I_{diff}}(s)$, where s is the distance travelled from the source. To simplify the analysis of our images we make the assumption that a photon retains its directional memory and polarisation until it undergoes N_d scattering events. This component of the flux which retains its initial polarisation, is the one responsible for the formation of the polarisation retaining image and is denoted by $\mathbf{I_{pol}}(s) = 1 - \mathbf{I_{diff}}(s)$. Undoubtedly this is an oversimplification but as we shall see later it yields excellent order-of-magnitude estimates. Figure 9 shows a semilogarithmic plot of $\mathbf{I_{pol}}(s)$ as a function of s. The dashed line is the diffusion theory prediction for the fraction of the incident flux that is not randomised; $\exp(-s/l^*)$. The figure shows the effect of the scattering anisotropy on the rate at which the snake photons are converted to a diffusive flux. The curves marked 'a', 'b' and 'c' represent scattering anisotropies of 0.1, 0.4 and 0.8 respectively. At short distances, due to the strong forward scattering for the highly anisotropic scatterers, we see that the flux is barely diffused for a length of $2l^*$. For the isotropic scatterers though, the rate of conversion is much faster. However, irrespective of the value of g, we find that the diffusion approxmation greatly underestimates the snake photon intensity.

A more interesting and counterintuitive feature is seen in the tail of the distributions. After traversing a depth $\sim 3l^*$, $\mathbf{I_{pol}}(s)$ shows an exponential roll-off for all values of g. However, surprisingly, the tail of curve 'a' flattens out around $8l^*$ unlike that of curve 'c' for $g = 0.8$. One would have expected rather that a higher scattering anisotropy would lead to a longer persistence length. This leads us to the surprising conclusion that one can image deeper into a turbid medium with isotropic scatterers than is possible through a medium where the scatterers are anisotropic. We comment on this point in a more quantitative manner in the next section.

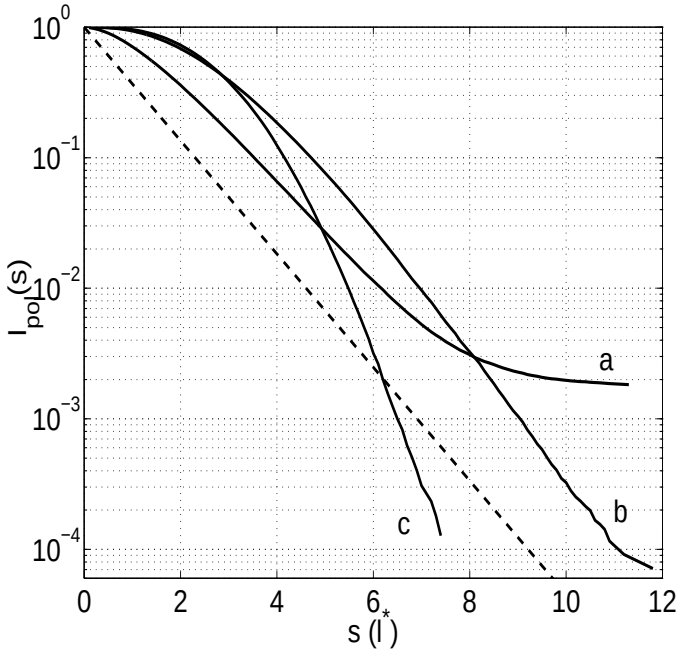

Figure 9: Semilogarithmic plot of $\mathbf{I_{pol}(s)}$, shown here as a function of s, the depth travelled into the medium, and compared for different scattering anisotropies g. The dashed line is the diffusion theory prediction for $\mathbf{I_{pol}}(s)$, while the curves marked 'a', 'b' and 'c' are obtained for $g = 0.1$, 0.4 and 0.8 respectively. The depth s is measured in units of l^*.

5 Putting it all together

We are now in a position to construct a model that provides quantitative agreement with our experiments. Consider a collimated beam of photons entering a slab of scattering medium of thickness L. The fraction of photons that are transmitted, according to the diffusion approximation, is given by the diffuse transmission probability T_d [21],

$$T_d = \frac{1 + z_e}{(L/l^*) + 2z_e} \tag{2}$$

where $z_e = 2l^*/3$ is the extrapolation length outside the sample, at which the diffuse flux extrapolates to zero [22]. For $L < 3l^*$ the diffuse transmission probability given by eq.(2), deviates significantly from experiment [20]. However, we choose to ignore this as we wish to obtain estimates for imaging through thick scattering slabs where eq.(2) is valid. Out of the fraction of the incident intensity that is transmitted, a fraction $\mathbf{I_{diff}}(\mathrm{L})$ is randomised and is converted to a diffuse flux. The remaining fraction $1 - \mathbf{I_{diff}}(\mathrm{L})$ is the polarisation preserving component $\mathbf{I_{pol}}(\mathrm{L})$ responsible for the formation of the image. The quantity $\hat{\mathbf{I}}_{\mathbf{diff}}$ is the diffuse flux that emerges normally from the cuvette and is imaged onto the detector .The rest of the diffuse flux which emerges at other angles is rejected by the aperture placed in front of the CCD camera. Whether or not an image is detected depends on two factors, the dynamic range of the detector, and the relative intensities of $\mathbf{I_{pol}}(\mathrm{L})$ and $\hat{\mathbf{I}}_{\mathbf{diff}}$.

The image bearing intensity incident upon the CCD array is simply $\mathbf{I_{pol}}(\mathrm{L})T_d$ since this flux is assumed to emerge normally from the sample. The diffuse flux $\hat{\mathbf{I}}_{\mathbf{diff}}$ that emerges normal to the cuvette

and is imaged onto the CCD is controlled by the aperture **PH**. It can be shown that for an aperture of diameter d_a placed in the focal plane of a lens of focal length f, the angular acceptance of the lens is equal to the angle subtended by the aperture as measured from the centre of the lens [23]. In our experiment, an aperture with a diameter of 1.3mm was placed at the focal plane of a lens with a focal length of 90 mm. Thus, the acceptance angle δ of the limiting aperture is ~ 0.83 degrees.

To quantitatively determine the fractions of the various fluxes making up the transmitted intensity, it only remains for us to estimate the fraction of the diffuse intensity that is scattered out from the cuvette within the acceptance angle δ of the lens aperture system. We use a result due to Durian for the angular distribution of diffusely transmitted light [21]. The expression obtained, based on the diffusion approximation, for the probability for a photon to be transmitted between the angles $\cos^{-1}(\mu)$ and $\cos^{-1}(\mu + d\mu)$ from the exterior normal is given by

$$P(\mu) = \frac{z_e\mu + \mu^2}{\frac{z_e}{2} + \frac{1}{3}} \tag{3}$$

In deriving this expression, it has been assumed that there is no refraction at the walls of the cuvette and that the boundary reflectivity is independent of angle and polarisation. A more detailed expression has also been derived [24] which includes these effects. However, since we are attempting only an order-of-magnitude estimation, we omit these details. Integrating $P(\mu)$ from $-\delta/2$ to $\delta/2$, we find the fraction of the diffuse flux emerging within the acceptance angle of the lens aperture system to be ~ 0.007. However, since this randomly polarised intensity has to pass through a polariser before reaching the CCD array, only half the flux is transmitted resulting in $\hat{\mathbf{I}}_{\mathbf{diff}} \sim 3.5 \times 10^{-3} \cdot \mathbf{I}_{\mathbf{diff}}(\mathrm{L}) \cdot T_d$. In summary, for a unit intensity incident on the scattering medium, the total transmitted intensity T_d may be partitioned as follows : (a) polarisation retaining fraction of the transmitted intensity = $\mathbf{I}_{\mathbf{pol}}(\mathrm{L}) \cdot T_d$; (b) randomised fraction of the transmitted intensity = $\mathbf{I}_{\mathbf{diff}}(\mathrm{L}) \cdot T_d$; and, (c) fraction of the randomised transmitted intensity incident on the detector = $\hat{\mathbf{I}}_{\mathbf{diff}} \sim 3.5 \times 10^{-3} \cdot \mathbf{I}_{\mathbf{diff}}(\mathrm{L}) \cdot T_d$. Figure 10 shows a plot of these fractions for scatterers with $g = 0.45$, the anisotropy of the particles used in the experiment. Curve 'a' is the diffuse transmitted fraction of the total incident intensity T_d. Curves 'b' and 'c' are the polarisation preserving intensity $\mathbf{I}_{\mathbf{pol}}(\mathrm{s})$, and the randomised intensity selected by the aperture $\hat{\mathbf{I}}_{\mathbf{diff}}(\mathrm{s})$ respectively, and s is the distance travelled into the scattering medium measured in units of the transport mean free path.

Finally, we must obtain the criterion by which we can decide whether an image may be extracted or not. When the polariser and analyser are crossed, only the diffuse intensity is seen by the CCD and this is the lowest intensity that will be observed. When they are parallel, the CCD records the sum of the diffuse and polarisation preserving intensities. Thus, the intensity time series for any pixel fluctuates between these two values. However, with an 8 bit detection system such as ours, the ripple in the intensity above the baseline due to the rotating polariser, will not be detected when the amplitude of the ripple is less than $\frac{1}{256}$ of the baseline intensity. In practice though, for optically thick samples, the baseline is not actually at zero when the polarisers are crossed because a large diffuse flux is present and this further reduces the available dynamic range of the detector. Therefore, the limit of detection in our experiment is reached when $\mathbf{I}_{\mathbf{pol}}(\mathrm{s}) \leq \frac{1}{256}\hat{\mathbf{I}}_{\mathbf{diff}}(\mathrm{s})$, assuming that the entire dynamic range is available at all τ.

Figure 11 shows a semilogarithmic plot of the fluxes $\mathbf{I}_{\mathbf{pol}}(\mathrm{s})$ and $\hat{\mathbf{I}}_{\mathbf{diff}}(\mathrm{s})$ for three values of g. The curves marked 'a', 'b' and 'c' refer to g values of 0.1, 0.45 and 0.9 respectively. The dashed line represents the intensity level below which the dynamic range of the detector is insufficient to record an image. Curves 'a' and 'c' do not intersect with the dashed line, while curve 'b' comes very close

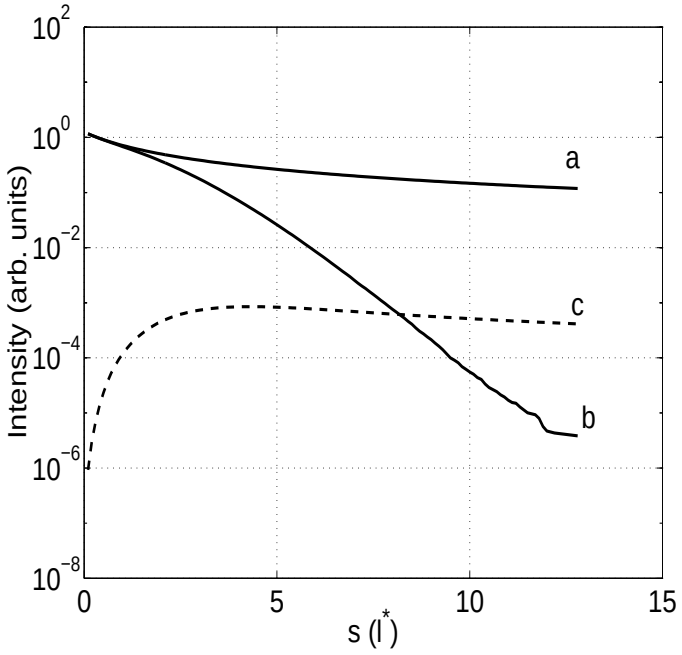

Figure 10: The total transmitted intensity T_d, the polarisation preserving fraction $\mathbf{I_{pol}}(\mathrm{s}) \cdot T_d$, and the normally emerging diffuse component selected by the aperture $\hat{\mathbf{I}}_{\mathbf{diff}}$, are shown for varying slab thicknesses s. The curves are obtained for $g = 0.45$, the anisotropy of the scatterers used in the experiment. The fractions are calculated assuming that a beam of unit intensity is incident on the medium. Curves 'a', 'b' and 'c' represent T_d, $\mathbf{I_{pol}}(\mathrm{s}) \cdot T_d$, and $\hat{\mathbf{I}}_{\mathbf{diff}}$ respectively.

to it. The reason is that the largest simulation we can perform can propagate 10^6 photons and we have insufficient data at large depths to exactly determine the point of intersection. However, the trends are clearly discerned. Curve 'b', which represents a g value of 0.45, similar to our experiment, is seen to intersect curve 'd' at $\sim 13l^*$. Experimentally, we find our limit of visibility to be at $\sim 10l^*$. Given that the dynamic range is greatly reduced at large τ and that at high gain the detector is very sensitive to stray light, this is in good agreement with our model.

We had previously commented, while discussing the results of our simulations shown in Fig.9, on the rate at which the number of polarisation preserving photons in the medium decreased with increasing depth. It was seen surprisingly, that the input beam was converted to a diffuse flux more rapidly with increasing g. We now examine the consequences that this rate of decay has on the image visibility assuming an imaging arrangement such as the one we have used. We see interestingly that for $g = 0.9$, the curve steeply drops towards the limit of visibility near $s = 7l^*$, while the limit of visibility for $g = 0.45$ is approximately $13l^*$. For $g = 0.1$, the curve flattens out and is nearly constant upto $s = 13l^*$. We have been unable to obtain data beyond this depth. However, it indicates that both the depth upto which snake photon imaging may be performed, and the quality of the image as determined by the parameter $\mathbf{R}$ are both significantly larger and better for isotropic scatterers.

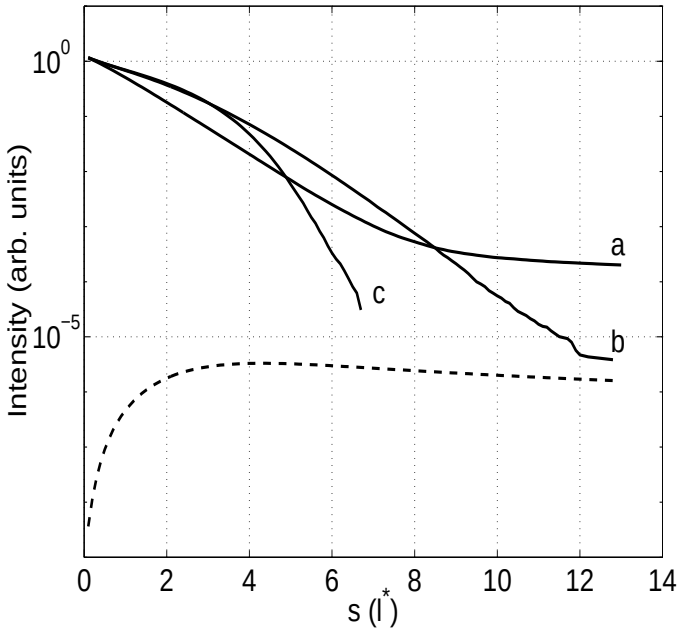

Figure 11: Semilogarithmic plot comparing the fraction of the transmitted intensit y $\mathbf{I_{pol}}(s) \cdot T_d$, that still retains its original state of polarisation after travelling a distance s into the medium, for different values of the scattering anisotropy g. The dashed line is the is the limit of visibility set by the dynamic range of the detector as $\frac{1}{256}\hat{\mathbf{I}}_{\mathbf{diff}}(\mathrm{s})$. The point of intersection of the dashed line with any of the curves is the optical depth beyond which snake photon imaging is not possible. The curves marked 'a', 'b' and 'c' represent scattering anisotropies of 0.1, 0.45 and 0.9 respectively.

5.1 Assumptions and approximations

A crucial input to our estimation of the image visibility has been the calculation of the fraction of the snake component that has been randomised, and obtaining consequently, the fraction that is polarisation preserving. In our simulation, for N photons that are launched from the origin, a number $N_{diffuse}$ of those photons undergo N_d scattering events .The randomisation probability is obtained by normalising the randomisation length histograms by $N_{diffuse}$. However not all these photons that are launched *and* undergo N_d scattering events are transmitted. While the simulation stops propagating these trajectories after N_d events, some of them are still backscattered. Therefore, our calculation of the polarisation preserving transmitted intensity, $\mathbf{I_{pol}}(\mathrm{L}) \cdot T_d$, tacitly assumes that these photons are all transmitted, an assumption that is not strictly valid. Yet, we find the agreement with experiment to be good enough to permit us to make this simplifying approximation. Further work is in progress to study in greater detail the path length distribution of these randomised photons to understand why this error is not significant.

Another bias that has been implicit in all our discussion so far has been that we have not demanded accuracy of our results at low optical densities. We feel that the analysis of the scattering of light in optically thin slabs is simple since almost all the light is transmitted virtually undeviated despite some scattering. Thus, although the transmission coefficient T_d is inaccurate at low optical densities, and corrected versions are available for this expression [16], we have not used them, both to keep matters simple as well as because our main focus is in the regime $L > 4l^*$ where the diffuse flux is large.

6 Conclusions and Comments

From experiments using particles with $g = 0.45$, we have found that imaging with quasi-ballistic light is possible to depths greater than that predicted by diffusion theory. To summarise our findings, we begin with our results concerning the crossover from the quasi-ballistic to the diffuse regime. We have classified as 'diffuse', a photon that has lost all memory of its initial direction of propagation. This angular memory is quantified in terms of the angular correlation function $C(j) = \langle \hat{\mathbf{n}}(0) \cdot \hat{\mathbf{n}}(j) \rangle$. To our knowledge, such a definition of what constitutes a diffuse photon has not been used before and we find that it is highly instructive and offers greater insight into the way photons are converted from quasi-ballistic to diffusive transport We have calculated, as a function of the scattering anisotropy, the number of scattering events N_d for $C(j)$ to fall to zero. We find that, contrary to the assumption implicit in diffusion theory, that a photon undergoes approximately $n = l^*/l_s$ scattering events before it is randomised, it actually takes many more scattering events for the photon to be randomised, as can be seen from Table 1 and Fig. 8. However, calculating N_d does not provide information on the typical length scale on which angular correlation is lost.

To understand the distribution of lengths over which photons are directionally randomised, we have used random walk simulations and obtained the path length distribution of the snake photons. We have assumed, that until a photon has undergone N_d scattering events, it retains all memory of its initial polarisation. Drastic though this may seem at first sight, it surprisingly explains our experimental results very well. Further work is in progress to calculate the pathlength distributions of these snake photons, with polarisation taken into account, in order to understand this approximation better.

We observe that it takes upto a thickness of about $6 - 8$ transport mean free paths, depending on g, before practically the entire snake component is randomised .Thus we are able to explain the observation that diffusing wave spectroscopy, when used in the transmission geometry, provides accurate results only when slab thicknesses exceed this limit [1, 15]. The distribution of the randomisation lengths is the central result of our work. It shows that image bearing photons are present in the medium to a depth much greater than that predicted by diffusion theory where there is an exponential conversion, on a length scale of the order of l^*, to diffusive transport. Thus our simulations explain why the diffusion approximation, which models the source of diffusing photons as a delta function at a depth of l^* inside the medium, is inaccurate for slab thicknesses less than $6 - 8l^*$.

The abrupt reduction in $\mathbf{R}$ is now simple to explain and is dependent on the dynamic range of the detector. In our experiment, we use an 8-bit, 256 grayscale level CCD camera. So, as long as $\mathbf{I_{pol}}(s)$ is greater than 256 times the diffuse intensity $\hat{\mathbf{I}}_{\mathbf{diff}}(\mathrm{s})$ incident on the detector, the ratio remains at 0.5. As soon $\mathbf{I_{pol}}(s) \leq \hat{\mathbf{I}}_{\mathbf{diff}}(\mathrm{s})$ an exponential fall in visibility is observed. After the limit of visibility is crossed, the detector has insufficient dynamic range to distinguish the oscillating intensity due to the snake component from the diffuse background. The detector sees a constant intensity and R is a constant once again.

Finally, we address our aim of placing limits on the depths to which direct imaging into a turbid medium is possible. While we have constantly used the word 'imaging' so far, we are actually looking at the transmission of photons through a random medium and the extent to which they preserve their original directions of propagation. In, for example, a medical diagnostic situation, the limits we have found would strictly be valid only for making shadowgrams of inclusions whose scattering characteristics are different from the bulk medium in which they are embedded. However, multiple shadows used in conjunction with standard inversion procedures such as the backpropagation algorithm

[25] can be used to create three dimensional 'images' of inclusions in the medium. These too are not strictly images, in that we cannot detect surface features on an embedded object. We can only detect the outlines of the embedded object. Our simulations show that for the limit of visibility, assuming an experimental setup such as ours, maximum imaging depths range from $\sim 7l^*$ for $g = 0.9$ to $\sim 13l^*$ for $g = 0.45$. For $g = 0.1$, our simulations are unable to determine the limit of visibility. We expect that it lies significantly greater than $13l^*$. In fact [11] suggests that it lies beyond $30l^*$. We find this result both surprising and counterintuitive that the maximum imaging depth decreases with increasing scattering anisotropy. We do not yet understand the origin of this effect. It should be noted that by reducing the size of the aperture **PH**, or choosing a detector with a greater dynamic range, the limit of visibility may be extended. Before closing we would like to comment that this last result is consistent with the observations of Bizheva *et al.* [26] that were published at the time that our manuscript was being prepared. Similar to the work of Kaplan *et al.*[20], Bizheva *et al.* also study the transition to DWS, but by means of an optical coherence tomography technique. They also find that, "for smaller scattering anisotropy diffusing light is detected after a greater number of photon random walks in the sample", and "the transition to the light diffusion regime occurs at shorter path lengths for media with higher scattering anisotropy".

Acknowledgements

We thank the Supercomputer Education and Research Centre (SERC) at the Indian Institute of Science for computational facilities. AKS thanks the Raman Research Institute for a visiting professorship. AKS and VG[1] thank the Board of Research in Nuclear Sciences, India, for financial assistance.

References

[1] D. J. Pine, D. A. Weitz, J. X, Zhu and E. Herbolzheimer, J. Phys. (Paris), **51**, 2101 (1990).

[2] D. A. Boas, L. E. Campbell and A. G. Yodh, Phys. Rev. Lett. **75**, 1855 (1995).

[3] M. Heckmeier, S. E. Skipetrov, G. Maret and R. Maynard, J. Opt. Soc. Am. A**14**, 185 (1997).

[4] P. M. den Outer, Th. M. Nieuwenhuizen and Ad Lagendijk, J. Opt. Soc. Am. A**10**, 1209 (1993).

[5] A large number of references may be found in *Time resolved imaging and diagnositics in medicine*, J. G. Fujimoto ed., Optics and Photonics News, October 1993.

[6] S. G. Demos and R. R. Alfano, Optics Lett. **21**, 161 (1996).

[7] S. G. Demos and R. R. Alfano, Appl. Optics **36**, 150 (1997).

[8] S. P. Morgan, M. P. Khong and M. G. Somekh, Appl. Optics **36**, 1560 (1997).

[9] J. M. Schmitt, A. H. Gandjbakhche and R. F. Bonner, Appl. Optics **31**, 6535 (1992).

[10] O. Emile, F. Bretenaker and A. Le Floch, Optics Lett. **21**, 1706 (1996).

[11] H. Ramachandran and A. Narayanan, Optics Comm. **154**, 255 (1998).

[1]Author for correspondence, e-mail : vgopal@physics.iisc.ernet.in

[12] C. F. Bohren and D. R. Huffman, *Absorption and Scattering of Light by small Particles*, Appendix-A, (Wiley Interscience, New York, 1983). Also available by anonymous ftp from : ftp://astro.princeton.edu/draine/scat/bhmie

[13] *The Feynman lectures on Physics*, (Addison Wesley, New York, 1965). See section 32-5.

[14] A simple derivation of the transport mean free path in analogy with the persistence length of a polymer chain may be found on p 322 in : D. J. Pine, D. A. Weitz, G. Maret, P. W. Wolf, E. Herbolzheimer and P. M. Chaikin, *Scattering and Localization of Classical Waves in Random Media*, (P. Sheng ed., World Scientific Publishing, (1990)).

[15] D. J. Durian, Phys. Rev. E **51**, 3350 (1995).

[16] D. J. Durian, Appl. Opt. **34**, 7100 (1995).

[17] Let $\mathbf{x}$ denote the series of all 512 time ordered values taken by the pixel $P_k(i,j)$ $(k = 1, 512)$ which is given as an input to the FFT routine. We choose the Fourier expansion of $\mathbf{x}$ to be : $\mathbf{x}(n) = A_0 + \sum_{l=1}^{N/2} \left[A_l \cos(\frac{2\pi ln}{N}) + B_l \sin(\frac{2\pi ln}{N}) \right]$; $(n = 1, 512, N = 512)$
where $A_0 = \frac{2}{N} \sum_{l=1}^{N} \mathbf{x}(l)$

[18] Ping Sheng, *Introduction to Wave Scattering, Localization, and Mesoscopic Phenomena*, (Academic press, 1995), page 174, problem 4.5.

[19] W. H. Press, S. A. Teukolsky, W. T. Vetterling and B. P. Flannery, *Numerical Recipes in FORTRAN - The art of scientific computing*,(Cambridge 1992).

[20] P. D. Kaplan, M. H. Kao, A. G. Yodh and D. J. Pine, Appl. Opt. **32**, 3828 (1993).

[21] D. J. Durian, Phys. Rev. E **50**, 857 (1994).

[22] P. M. Morse and H. Feshbach, *Methods of Theoretical Physics*, vol. I, (McGraw Hill, New York, 1953) (See sec. 2.4).

[23] See the description of the searchlight on p 219 in :
M. V. Klein and T. Furtak, *Optics*, (McGraw Hill, New York).
The searchlight consists of a Lambertian source of a finite radius placed at the focus of a lens. A Lambertian source emits diffuse radiation with equal intensity in all directions. This is a good approximation for a turbid medium emitting diffuse radiation. Simply by reversing the rays in the searchlight, we obtain our situation of a lens bringing diffuse rays to a focus with an aperture placed in the focal plane of the lens.

[24] M. U. Vera and D. J. Durian, Phys. Rev. E **53**, 3215 (1996).

[25] L. L. Kalpaxis, L. M. Wang, P. Galland, X. Liang, P. P. Ho and R. R. Alfano, Optics Lett. , **18**, 1691 (1993).

[26] Kostadinka K. Bizheva, Andy M. Siegel and David A. Boas, Phys. Rev. E **58**, 7664 (1998).